Editors' Suggestion | Featured in Physics

High Compression Blue-Detuned Magneto-Optical Trap of Polyatomic Molecules

Christian Hallas,* Grace K. Li, Nathaniel B. Vilas, Paige Robichaud, Loïc Anderegg, and John M. Doyle
Department of Physics, Harvard University, Cambridge, Massachusetts 02138, USA
and Harvard-MIT Center for Ultracold Atoms, Cambridge, Massachusetts 02138, USA

(Received 9 May 2024; accepted 18 December 2025; published 1 April 2026)

We demonstrate a blue-detuned magneto-optical trap (MOT) of a polyatomic molecule, calcium monohydroxide (CaOH). We identify a novel MOT frequency configuration that produces high spatial compression of the molecular cloud. This high compression MOT achieves a cloud radius of 59(5) μm and a peak density of $8(2) \times 10^8$ cm^{-3}. We experimentally compare several blue-detuned MOT schemes for CaOH and find good agreement between our data and Monte Carlo simulations.

DOI: 10.1103/w9qc-rczf

Ultracold molecules are novel quantum systems with rich internal level structures and large intrinsic electric dipole moments, which make them promising platforms for pursuing a wide range of scientific applications. These include quantum information processing [1–7], quantum simulation [8–10], searches for physics beyond the Standard Model [11–13], and studies of quantum chemistry [14] and collisions [15]. Over the last decade, significant experimental effort has been made in developing laser cooling and trapping techniques for molecules. Magneto-optical traps (MOTs) have been realized for a number of molecular species and, as with atoms, the MOT has become an important tool for rapid spatial compression and cooling of molecules to submillikelvin temperatures [16–21]. In combination with sub-Doppler laser cooling techniques [17,21–25], the development of molecular MOTs has enabled the loading of laser-cooled molecules into conservative optical traps [26–28]. Recently, tweezer arrays of individual molecules, including polyatomic molecules, have also been demonstrated with laser-cooled molecules [29–31]. Several milestones toward the above applications have been realized, e.g., studies of molecular collisions at ultracold temperatures [15,32], the demonstration of entanglement between individual molecules [30,33], and sideband cooling to the motional ground state [34,35].

Conventional molecular MOTs rely on Doppler cooling and trapping forces achieved by optically cycling on an electronic transition using "red-detuned" MOT light, i.e., the MOT light frequency is smaller than the resonance frequency of the transition. Rotationally closed cycling is accomplished by driving so-called type-two transitions with $J \geq J'$, where J (J') is the quantum number for the total angular momentum of the ground (excited) electronic state [36]. At low molecular velocities, type-two systems exhibit strong Sisyphus-like forces, which for red-detuned light give rise to heating [37]. Compared with typical atomic MOTs, which drive type-one transitions with $J < J'$, red-detuned molecular MOTs ("red MOTs") therefore have relatively high temperatures (∼1 mK) and low spatial confinement (cloud sizes of ∼1 mm) [16,19–21]. The weak compression of red molecular MOTs has limited the loading of molecules into conservative optical traps to a few percent. Higher molecular number densities are desirable for a number of scientific goals and, in particular, for any experiments involving collisions, including evaporative cooling to quantum degeneracy. With an eye toward improving molecular MOTs, blue-detuned MOTs were proposed [38] and demonstrated using Rb atoms [39] by Tarbutt and co-workers. With blue-detuned MOT light, heating turns into Sisyphus-like cooling for molecules at low velocities. Recently, blue-detuned MOTs ("blue MOTs") were demonstrated for diatomic molecules [40–42] with great success. Blue MOTs realized with diatomic molecules have achieved both lower temperatures and higher densities compared to red-detuned molecular MOTs.

In this Letter, we demonstrate a blue MOT for a polyatomic molecule, calcium monohydroxide (CaOH), and identify a MOT light frequency scheme for CaOH that realizes higher spatial compression than existing blue molecular MOTs. In this "1 + 2" scheme, a single-frequency light beam addresses one resolved ground state and an additional pair of light beams address a different resolved ground state. Within the pair, the beams have opposite polarizations, with their frequencies separated by less than the MOT transition linewidth. This approach is in contrast with previously realized blue molecular MOT schemes, which use at most one frequency component per ground state. Using our 1 + 2 MOT scheme, we realize a peak molecular density for CaOH of $8(2) \times 10^8$ cm^{-3}, with ∼2900 molecules trapped at a cloud radius of 59(5) μm. This density is more than 2 orders of magnitude larger than we achieve with a red MOT for CaOH [21] and is the highest density reported for a molecular MOT to date.

*Contact author: christianhallas@g.harvard.edu

 © 2026 American Physical Society

The temperature of the $1+2$ MOT is 170(10) μK, slightly above the Doppler temperature for CaOH of 140 μK. To compare the $1+2$ MOT scheme with existing blue MOT schemes, we implement a "$1+1$" MOT scheme for CaOH, using the standard single-frequency component for each of the two resolved ground states. Significantly weaker compression is found for the $1+1$ scheme, realizing a density of $5(1)\times10^7$ cm^{-3}. The use of a $1+2$ scheme was motivated by our studies of molecular MOTs using Monte Carlo simulations based on the stochastic Schrödinger equation [43]. We find good agreement between our experimental data and the simulation results.

In our experiment, CaOH molecules produced from a cryogenic buffer gas beam source are first radiatively slowed and then captured in a red-detuned radio-frequency (rf) MOT, which is created using MOT beams with frequencies less than the frequency of the $\tilde{A}^2\Pi_{1/2}(J'=1/2)\leftarrow\tilde{X}^2\Sigma^+(N=1)$ electronic transition. (Since blue-detuned light gives rise to Doppler heating around the MOT capture velocity, blue MOTs do not provide initial capture and cooling.) The CaOH level structure and red MOT laser configuration are shown in Fig. 1(a). The $|N=1\rangle$ state contains two spin-rotation states, $|J=1/2\rangle$ and $|J=3/2\rangle$, split by ∼51 MHz. Each spin-rotation state is further split into a pair of hyperfine states spaced by ∼10 kHz in $|J=1/2\rangle$ and ∼1.5 MHz in $|J=3/2\rangle$. This splitting is unresolved compared to the linewidth of the MOT transition of $\Gamma=2\pi\times6.4$ MHz, and the red MOT light contains single-frequency components to address each spin-rotation component [Fig. 1(a)]. The slowing light used to bring CaOH molecules to the capture velocity of the red MOT contains additional laser frequencies that repump molecules from 12 excited vibrational states of $\tilde{X}^2\Sigma^+$ back into the cycling transition, resulting in a "photon budget" of ∼13 500 scattered photons per $1/e$ loss of the molecular population to unaddressed vibrational levels. These repumping lasers pass through the MOT region and remain active during the full experimental sequence. Further details of the red MOT, which is operating as an rf MOT, and its laser configuration and operation are in Ref. [21]. After the initial capture of molecules, the MOT magnetic field gradient is ramped from 8.5 to 23.6 G/cm. Following a 10 ms wait time where spatial compression takes place, the Gaussian rms width σ of the red MOT is measured to be 0.53(3) mm and the peak molecular density is $2.0(3)\times10^6$ cm^{-3}.

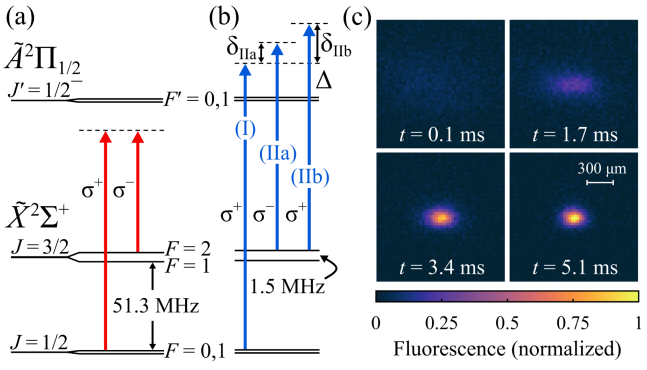


FIG. 1. (a) Level structure and laser configuration for the CaOH red (rf) MOT. (b) CaOH blue (dc) MOT laser configuration. The single-photon detuning is denoted by Δ, and the two-photon detunings for the two MOT beams addressing the $|J=3/2\rangle$ level are denoted by δ_{IIa}, and δ_{IIb}. (c) Images of the blue-detuned CaOH MOT taken with 2 ms *in situ* images following a compression time of t.

We realize a blue MOT by loading CaOH from a red MOT. First, the red MOT is switched off by turning off both the MOT light and the rf magnetic field in ∼130 μs. The MOT light beams are then turned back on in a "Λ-cooling" configuration to perform 1 ms of Λ-enhanced gray molasses cooling in free space, resulting in a molecular temperature of ∼34 μK. Details on Λ cooling for CaOH are in Ref. [27]. This Λ-cooling step prevents the molecules from leaving the MOT region during the time when the blue MOT is turned on and ensures that the molecules are within the relatively lower capture velocity of the blue MOT. The blue MOT is then created by switching the MOT laser configuration to the one shown in Fig. 1(b) and linearly ramping up a dc magnetic field in 4 ms. We observe negligible molecule loss during transfer to the blue MOT. In the blue MOT laser configuration, a single-frequency component (I), blue-detuned from the MOT transition by Δ, addresses $|J=1/2\rangle$ while two closely spaced frequency components of opposite polarization, denoted by (IIa) and (IIb), address $|J=3/2\rangle$. Referenced to $|J=3/2,F=2\rangle$, the detunings of (IIa) and (IIb) are $\Delta+\delta_{\mathrm{IIa}}$ and $\Delta+\delta_{\mathrm{IIb}}$, respectively, where δ_{IIa} and δ_{IIb} are the two-photon detunings for the (IIa) and (IIb) components with respect to (I). This configuration with both (I) and the (IIa)-(IIb) pair is referred to as the $1+2$ scheme.

Figure 1(c) shows *in situ* images taken throughout the compression of the molecular cloud while the $1+2$ MOT light is applied. The ramped (axial) magnetic field gradient is $B_z'=82$G/cm. The frequency parameters for the MOT light are $\Delta=7.6$, $\delta_{\mathrm{IIa}}=-1.0$, and $\delta_{\mathrm{IIb}}=0.75$ MHz and were chosen to maximize the compression of the molecular cloud. We note that, since $|J=3/2,F=1\rangle$ is only ∼1.5 MHz lower in energy compared to $|J=3/2,F=2\rangle$, the two-photon detunings with respect to this state are of a similar scale, though negative for both (IIa) and (IIb). The total $1+2$ MOT light intensity is ramped linearly from $I=30.0$ to $I=23.4$ mW/cm^2 during the magnetic field ramp. The fractions of the total intensity among the three frequency components are 37%, 28%, and 35% for (I), (IIa), and (IIb), respectively. The $1+2$ MOT is fully compressed after 5 ms and reaches a final size of $\sigma=59(5)$ μm. Using the time-of-flight expansion method, the molecular temperature is measured to be $T=170(10)$ μK. We observe a peak number density of $n_0=8(2)\times10^8$ cm^{-3} and a phase-space

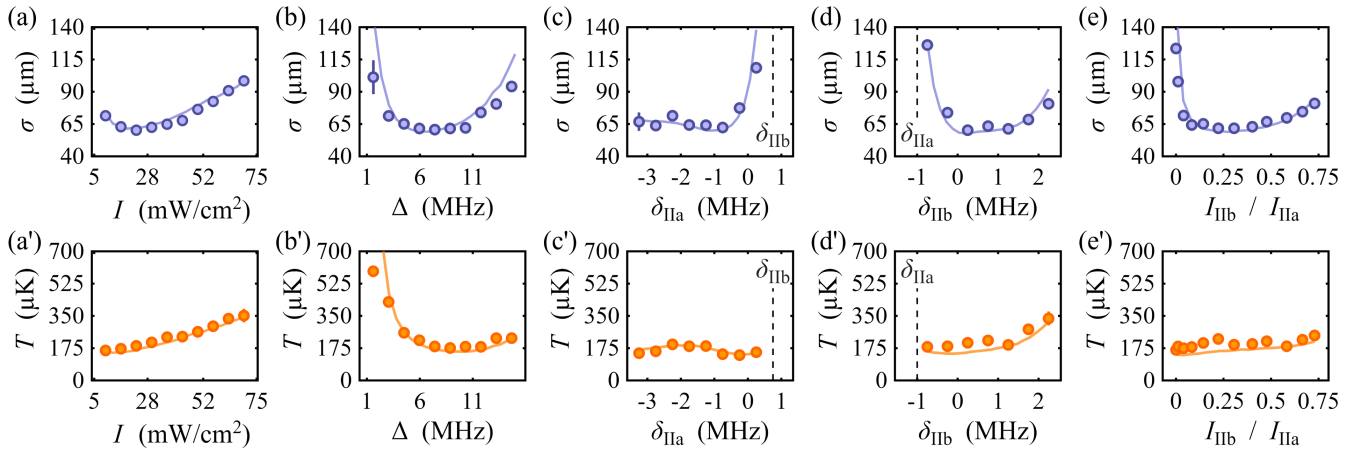


FIG. 2. $1+2$ MOT (a)–(e) width σ and (a')–(e') temperature T following 5 ms compression, as a function of (a),(a') total intensity I; (b),(b') one-photon detuning Δ; (c),(c') two-photon detuning of the (IIa) component δ_{IIa}; (d),(d') two-photon detuning of the (IIb) component δ_{IIb}; (e),(e') intensity ratio between (IIb) and (IIa) (with fixed total intensity I and ratio $I_{\mathrm{I}}/I_{\mathrm{IIa}} = 1.32$). The fixed parameters for each scan are $I = 36.5\ \mathrm{mW/cm^2}$, $\Delta = 7.6$ MHz, $\delta_{\mathrm{IIa}} = -1$ MHz, $\delta_{\mathrm{IIb}} = 0.75$ MHz, and $I_{\mathrm{IIb}}/I_{\mathrm{IIa}} = 1.25$. The MOT magnetic field gradient is 82G/cm. Solid curves are simulation results.

density of $4(1) \times 10^{-9}$. Details on the size and temperature measurements are given in Supplemental Material [44]. After the $1+2$ MOT compression, ~60% of the molecules that were in the red MOT remain, corresponding to ~2900 molecules. This loss is almost entirely from branching losses to vibrational dark states during photon cycling due to the finite photon budget. Given our scattering rate of $0.90(3) \times 10^6\ \mathrm{s^{-1}}$ and a photon budget of 13500 photons, this loss can be estimated theoretically as $e^{-0.9\times10^6\ \mathrm{s^{-1}}\times 5\ \mathrm{ms}/13500} \approx 71\%$.

We quantify the cooling and trapping forces in the MOT by modeling the MOT as a damped harmonic oscillator with force $F = -\alpha v - kr$. Here r is position, v is velocity, α is the damping coefficient, and k is the spring constant. Using the equipartition theorem, the spring constant can be extracted from the size and temperature according to $k = k_B T/\sigma^2$ [39]. We find $k = 6(1) \times 10^{-19}\mathrm{N/m}$ for the $1+2$ MOT, which is more than an order of magnitude larger than spring constants achieved in previously demonstrated blue-detuned MOTs [40–42].

We further characterize the $1+2$ MOT by measuring the MOT width σ and temperature T as a function of several MOT parameters (Fig. 2). The intensity and single-photon detuning (Δ) data show clear minima in the MOT size [Figs. 2(a) and 2(b)], while the temperature is minimized at the lowest light intensity and for detunings $\Delta \gtrsim 7$ MHz [Figs. 2(f) and 2(g)]. We find that the $1+2$ MOT size has a strong dependence on δ_{IIa} and δ_{IIb} [Figs. 3(c) and 3(d)], with the smallest σ achieved for $\delta_{\mathrm{IIa}} < 0$ and $0 < \delta_{\mathrm{IIb}} < 1.5$ MHz. The most obvious effect, however, is that, when δ_{IIa} and δ_{IIb} are tuned close to each other, σ increases dramatically, i.e., the trapping force vanishes. The variation of the relative power ratio between (IIb) and (IIa) demonstrates that, as the intensity of (IIb) is increased from zero, the cloud size shrinks to the minimum size [Fig. 2(e)]. The temperature is relatively insensitive to both δ_{IIa} and δ_{IIb} as well as the intensity ratio between (IIa) and (IIb) [Figs. 2(h)–2(j)].

The experimentally observed variation of the $1+2$ MOT size and temperature are compared to numerical predictions from Monte Carlo simulations, shown in Fig. 2 as solid curves. Briefly, these simulations are performed by initializing CaOH molecules from position and velocity distributions coinciding with the Λ-cooled molecule cloud (following the red MOT) and then numerically solving the stochastic Schrödinger equation [43] for each molecule in the presence of the blue MOT light and fields. Simulated MOT sizes and temperatures are derived as a function of time from the solved trajectories. The simulation results show excellent agreement with the experimental data. Additional details on the simulations are provided in Supplemental Material [44].

We also create a blue MOT that employs laser frequency (I) and only one of either (IIa) or (IIb). We refer to these $1+1$ schemes as (A) using (I) and (IIa), and (B) using (I) and (IIb). A difference between (A) and (B) is that the

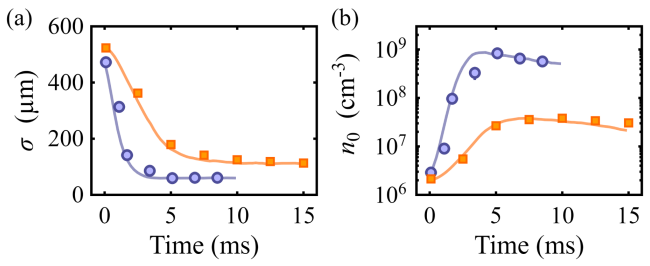


FIG. 3. (a) MOT width σ and (b) MOT peak number density n_0 versus compression time for the $1+2$ MOT (blue circles) and the $1+1$ (A) MOT (orange squares). Solid curves are simulation results.

polarization for the component addressing $|J = 3/2\rangle$ is reversed. The $1 + 1$ (A) MOT is the approach used in the blue MOTs created for YO and CaF and follows the conventional MOT configuration where the frequency separation between each of the components of the MOT light is significantly greater than the MOT transition linewidth [40,42]. We find significantly reduced spatial compression in both of the $1 + 1$ schemes. In Fig. 3, we compare the compressions of the $1 + 2$ and $1 + 1$ (A) MOTs. The compression predicted by the numerical simulations for the MOTs are shown as solid curves and are in excellent agreement with the experimentally observed sizes and compression timescales. At optimal parameters for compression, the $1 + 1$ (A) MOT achieves a final size of $\sigma = 110(4)$ μm after 15 ms of compression, which is ∼2× larger than the size achieved with the $1 + 2$ MOT. Similar to the $1 + 2$ MOT, the intensity is ramped from $I = 30.0$ to $I = 23.4$ mW/cm^2 over the first 4 ms, and the gradient is ramped to $B'_z = 82$G/cm. The intensity fractions between the components (I) and (IIa) are 56% and 44%, respectively, $\Delta = 7.6$ and $\delta_{\mathrm{IIa}} = -1.0$ MHz. The temperature of the $1 + 1$ (A) MOT is $T = 160(10)$ μK, which is similar to the temperature of the $1 + 2$ MOT. For the $1 + 1$ (A) MOT, $k = 1.8(1) \times 10^{-19}$ N/m, about ∼3.5× smaller than the spring constant for the $1 + 2$ MOT. The scattering rate of the $1 + 1$ (A) MOT is $0.7(1) \times 10^6$ s^{-1}, only ∼20% smaller than that of the $1 + 2$ MOT, so the large difference in spring constant implies that the $1 + 2$ MOT achieves a significantly larger restoring force per photon scattered. The peak molecular density of the $1 + 1$ (A) MOT is $n_0 = 5(1) \times 10^7$ cm^{-3}, a factor of ∼16 smaller compared to the $1 + 2$ MOT.

We note that, for the $1 + 1$ schemes, a strong dependence of the spatial compression of the MOT cloud on δ was observed [here δ refers to δ_{IIa} and δ_{IIb} for each of the respective $1 + 1$ (A) and (B) schemes]. We find for the $1 + 1$ (A) MOT that the sign of the MOT force is inverted around $\delta \approx 0$, transitioning from a trapping to an antitrapping force [44]. The strong dependence of the trapping force on δ, not only for the magnitude but also the sign of the force, suggests that two-photon effects may play an important role for the restoring forces achieved, perhaps in both the $1 + 1$ and $1 + 2$ MOTs. A more general investigation of the effects of two-photon resonances on MOT forces in type-two systems is warranted.

We characterize the performance of the $1 + 2$ MOT versus magnetic field gradient B'_z. As shown in Fig. 4(a), the compression continues to increase with gradient and, with $B'_z = 182$G/cm, the cloud is compressed to a size of 37(2) μm. The temperature remains roughly constant at ∼150–200 μK for the gradients explored. Figure 4(b) shows the lifetime τ of the molecular cloud at different gradients, measured by holding the compressed molecule cloud at each gradient for a varying duration and observing the number of remaining molecules. With a gradient of

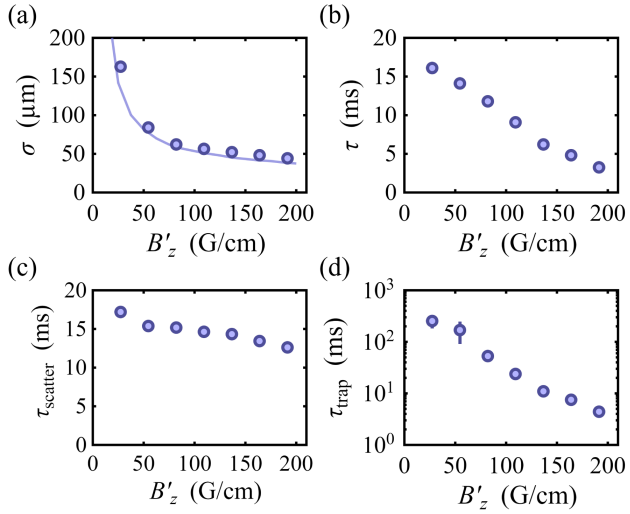


FIG. 4. $1 + 2$ MOT (a) width σ (solid line shows simulation results), (b) lifetime τ, (c) lifetime τ_{scatter} from branching loss to vibrational dark states, and (d) lifetime τ_{trap} from trap losses only, as a function of magnetic field gradient.

$B'_z = 82$G/cm, we measure $\tau = 11.8(2)$ ms. Because of our current (technologically limited) photon budget of ∼13500 photons, τ arises both from loss from branching into dark vibrational states (τ_{scatter}) and loss from molecules leaving the trap (τ_{trap}). The loss characterized by τ_{trap} is likely due to the finite depth of the trap, which becomes lower at higher gradients, as examined in Ref. [42]. The total lifetime is given by $\tau = (1/\tau_{\mathrm{scatter}} + 1/\tau_{\mathrm{trap}})^{-1}$. To isolate τ_{scatter} and τ_{trap}, we first measure the photon scattering rate R_{sc} at each gradient by repeating the same lifetime measurement but with a photon budget limited to ∼1400 photons such that $\tau \approx \tau_{\mathrm{scatter}} \ll \tau_{\mathrm{trap}}$. We calculate $\tau_{\mathrm{scatter}} = 13\,500/R_{\mathrm{sc}}$ as a function of gradient [Fig. 4(c)]. Using τ and τ_{scatter}, we also calculate $\tau_{\mathrm{trap}} = (1/\tau - 1/\tau_{\mathrm{scatter}})^{-1}$ as a function of gradient [Fig. 4(d)]. With $B'_z = 82$G/cm, we find $\tau_{\mathrm{trap}} = 53(7)$ ms, implying that, at this gradient, the lifetime is limited by τ_{scatter}. As the gradient is increased, the contribution from τ_{trap} becomes increasingly important, and with $B'_z \approx 125$G/cm, τ has roughly equal contributions from both τ_{scatter} and τ_{trap}. We note that the trap-limited lifetime τ_{trap} in the $1 + 1$ (A) MOT is significantly shorter than that of the $1 + 2$ MOT. For the $1 + 1$ (A) scheme, with $B'_z = 82$G/cm, we measure $\tau = 7(1)$ and $\tau_{\mathrm{scatter}} = 20(6)$ ms, which results in $\tau_{\mathrm{trap}} = 12(3)$ ms.

The mechanism underlying the improved compression of the $1 + 2$ MOT is not yet fully understood. However, our simulations suggest a possible explanation. When both of the (IIa) and (IIb) components are present, the MOT light addressing the $|J = 3/2\rangle$ state can, in each MOT axis, be decomposed into two slowly moving standing waves ("walking waves") with opposite circular polarizations and directions of motion. Because of spatially dependent

Zeeman shifts in the MOT, a molecule may preferentially interact with one of the opposing walking waves depending on its location. In a reference frame comoving with a walking wave, the molecule experiences Sisyphus-like cooling owing to the intensity gradient in the standing wave [37]. In the laboratory frame, the cooling force becomes a pushing force. By an appropriate choice of laser polarizations and magnetic field direction, this mechanism could provide a spatially dependent restoring force. We provide a detailed explanation of this hypothesized trapping mechanism in Supplemental Material [44] for a toy model with a single type-two transition, $|F=1\rangle \rightarrow |F'=0\rangle$, addressed by σ^+ and σ^- laser components that are close in frequency, as in the $1+2$ scheme. Numerical simulations of molecule trajectories show that, in this toy model, molecules concentrate around the speed of the walking waves during compression, indicating a cooling force in a moving frame. We suggest that a MOT relying on this mechanism may be referred to as a "conveyor belt MOT," since the walking waves act as conveyor belts that carry the molecules to the center of the trap. Motivated by this model, we have investigated the conveyor belt MOT effect in greater detail in a separate work, where we use optical Bloch equations [45] to derive force profiles for a range of similar toy models as well as full molecular level structures [51].

It is interesting to explore whether $1+2$ type schemes can lead to improved spatial compression in type-two MOTs for other molecules. Using our simulations, we develop promising MOT schemes similar to our $1+2$ MOT for CaF and YO. Details of these simulations are provided in Supplemental Material [44].

In summary, we have demonstrated a blue-detuned MOT for a polyatomic molecule, CaOH. We have devised and studied a $1+2$ MOT light scheme for CaOH that uses two closely spaced frequency components to address the same ground state and achieves significantly improved spatial compression compared to previously demonstrated blue-detuned molecular MOTs. Our results also suggest that two-photon effects can play an important role for MOT forces in type-two systems and that these effects should be taken into account when developing schemes for molecular MOTs. Based on numerical Monte Carlo simulations, similar $1+2$ MOT schemes should be applicable to other molecules such as CaF, YO, SrF, and SrOH, and possibly larger species. The spatial compression and concomitant increase in molecular number density offered by this blue-detuned MOT should improve the loading of optical traps. With better loading into optical dipole traps, one can expect that collisions of CaOH molecules in the bulk can be studied. Approaches have been suggested for realizing collisional shielding in CaOH, which could be implemented to achieve evaporative cooling [52]. Higher densities should also enable more robust loading of individual tweezer traps, which could aid in scaling to larger molecular array sizes.

Acknowledgments—We acknowledge Yicheng Bao and Jiaqi You for valuable discussions in developing the numerical Monte Carlo simulations. This work was supported by the AFOSR, NSF, ARO, DOE Quantum Systems Accelerator (QSA) and the Center for Ultracold Atoms (an NSF Physics Frontiers Center, under Grant No. PHY-2317134). G. K. L. and L. A. acknowledge support from the HQI, and P. R. acknowledges support from the NSF GRFP.

[1] D. DeMille, Phys. Rev. Lett. **88**, 067901 (2002).
[2] S. F. Yelin, K. Kirby, and R. Côté, Phys. Rev. A **74**, 050301 (R) (2006).
[3] K.-K. Ni, T. Rosenband, and D. D. Grimes, Chem. Sci. **9**, 6830 (2018).
[4] R. Sawant, J. A. Blackmore, P. D. Gregory, J. Mur-Petit, D. Jaksch, J. Aldegunde, J. M. Hutson, M. R. Tarbutt, and S. L. Cornish, New J. Phys. **22**, 013027 (2020).
[5] Q. Wei, S. Kais, B. Friedrich, and D. Herschbach, J. Chem. Phys. **135**, 154102 (2011).
[6] P. Yu, L. W. Cheuk, I. Kozyryev, and J. M. Doyle, New J. Phys. **21**, 093049 (2019).
[7] V. V. Albert, J. P. Covey, and J. Preskill, Phys. Rev. X **10**, 031050 (2020).
[8] A. Micheli, G. Brennen, and P. Zoller, Nat. Phys. **2**, 341 (2006).
[9] A. V. Gorshkov, S. R. Manmana, G. Chen, E. Demler, M. D. Lukin, and A. M. Rey, Phys. Rev. A **84**, 033619 (2011).
[10] M. L. Wall, K. R. A. Hazzard, and A. M. Rey, in *From Atomic to Mesoscale: The Role of Quantum Coherence in Systems of Various Complexities*, edited by S. Malinovskaya and I. Novikova (World Scientific, Singapore, 2015), Chap. 1, pp. 3–38.
[11] I. Kozyryev and N. R. Hutzler, Phys. Rev. Lett. **119**, 133002 (2017).
[12] I. Kozyryev, Z. Lasner, and J. M. Doyle, Phys. Rev. A **103**, 043313 (2021).
[13] E. B. Norrgard, D. S. Barker, S. Eckel, J. A. Fedchak, N. N. Klimov, and J. Scherschligt, Commun. Phys. **2**, 1 (2019).
[14] B. R. Heazlewood and T. P. Softley, Nat. Rev. Chem. **5**, 125 (2021).
[15] L. W. Cheuk, L. Anderegg, Y. Bao, S. Burchesky, S. S. Yu, W. Ketterle, K.-K. Ni, and J. M. Doyle, Phys. Rev. Lett. **125**, 043401 (2020).
[16] J. Barry, D. McCarron, E. Norrgard, M. Steinecker, and D. DeMille, Nature (London) **512**, 286 (2014).
[17] S. Truppe, H. Williams, M. Hambach, L. Caldwell, N. Fitch, E. Hinds, B. Sauer, and M. Tarbutt, Nat. Phys. **13**, 1173 (2017).
[18] H. Williams, S. Truppe, M. Hambach, L. Caldwell, N. Fitch, E. Hinds, B. Sauer, and M. Tarbutt, New J. Phys. **19**, 113035 (2017).
[19] L. Anderegg, B. L. Augenbraun, E. Chae, B. Hemmerling, N. R. Hutzler, A. Ravi, A. Collopy, J. Ye, W. Ketterle, and J. M. Doyle, Phys. Rev. Lett. **119**, 103201 (2017).
[20] A. L. Collopy, S. Ding, Y. Wu, I. A. Finneran, L. Anderegg, B. L. Augenbraun, J. M. Doyle, and J. Ye, Phys. Rev. Lett. **121**, 213201 (2018).

[21] N. B. Vilas, C. Hallas, L. Anderegg, P. Robichaud, A. Winnicki, D. Mitra, and J. M. Doyle, Nature (London) **606**, 70 (2022).
[22] L. W. Cheuk, L. Anderegg, B. L. Augenbraun, Y. Bao, S. Burchesky, W. Ketterle, and J. M. Doyle, Phys. Rev. Lett. **121**, 083201 (2018).
[23] L. Caldwell, J. A. Devlin, H. J. Williams, N. J. Fitch, E. A. Hinds, B. E. Sauer, and M. R. Tarbutt, Phys. Rev. Lett. **123**, 033202 (2019).
[24] T. K. Langin, V. Jorapur, Y. Zhu, Q. Wang, and D. DeMille, Phys. Rev. Lett. **127**, 163201 (2021).
[25] S. Ding, Y. Wu, I. A. Finneran, J. J. Burau, and J. Ye, Phys. Rev. X **10**, 021049 (2020).
[26] L. Anderegg, B. L. Augenbraun, Y. Bao, S. Burchesky, L. W. Cheuk, W. Ketterle, and J. M. Doyle, Nat. Phys. **14**, 890 (2018).
[27] C. Hallas, N. B. Vilas, L. Anderegg, P. Robichaud, A. Winnicki, C. Zhang, L. Cheng, and J. M. Doyle, Phys. Rev. Lett. **130**, 153202 (2023).
[28] T. K. Langin, V. Jorapur, Y. Zhu, Q. Wang, and D. DeMille, Phys. Rev. Lett. **127**, 163201 (2021).
[29] L. Anderegg, L. W. Cheuk, Y. Bao, S. Burchesky, W. Ketterle, K.-K. Ni, and J. M. Doyle, Science **365**, 1156 (2019).
[30] C. M. Holland, Y. Lu, and L. W. Cheuk, Science **382**, 1143 (2023).
[31] N. B. Vilas, P. Robichaud, C. Hallas, G. K. Li, L. Anderegg, and J. M. Doyle, Nature (London) **628**, 282 (2024).
[32] L. Anderegg, S. Burchesky, Y. Bao, S. S. Yu, T. Karman, E. Chae, K.-K. Ni, W. Ketterle, and J. M. Doyle, Science **373**, 779 (2021).
[33] Y. Bao, S. S. Yu, L. Anderegg, E. Chae, W. Ketterle, K.-K. Ni, and J. M. Doyle, Science **382**, 1138 (2023).
[34] Y. Lu, S. J. Li, C. M. Holland, and L. W. Cheuk, Nat. Phys. **20**, 389 (2024).
[35] Y. Bao, S. S. Yu, J. You, L. Anderegg, E. Chae, W. Ketterle, K.-K. Ni, and J. M. Doyle, Phys. Rev. X **14**, 031002 (2024).
[36] B. K. Stuhl, B. C. Sawyer, D. Wang, and J. Ye, Phys. Rev. Lett. **101**, 243002 (2008).
[37] J. Devlin and M. Tarbutt, New J. Phys. **18**, 123017 (2016).
[38] M. Tarbutt, New J. Phys. **17**, 015007 (2015).
[39] K. N. Jarvis, J. A. Devlin, T. E. Wall, B. E. Sauer, and M. R. Tarbutt, Phys. Rev. Lett. **120**, 083201 (2018).
[40] J. J. Burau, P. Aggarwal, K. Mehling, and J. Ye, Phys. Rev. Lett. **130**, 193401 (2023).
[41] V. Jorapur, T. K. Langin, Q. Wang, G. Zheng, and D. DeMille, Phys. Rev. Lett. **132**, 163403 (2024).
[42] S. J. Li, C. M. Holland, Y. Lu, and L. W. Cheuk, Phys. Rev. Lett. **132**, 233402 (2024).
[43] K. Mølmer, Y. Castin, and J. Dalibard, J. Opt. Soc. Am. B **10**, 524 (1993).
[44] See Supplemental Material at http://link.aps.org/supplemental/10.1103/w9qc-rczf, which includes Refs. [20,22,37,40,42,43,45–50].
[45] J. A. Devlin and M. R. Tarbutt, Phys. Rev. A **98**, 063415 (2018).
[46] C. Hallas, G. K. Li, N. B. Vilas, P. Robichaud, L. Anderegg, and J. M. Doyle, CaOH Blue MOT Simulations, GitHub repository, 2025, https://github.com/hallaschristian/CaOHBlueMOTSimulations.
[47] J. Dalibard, Y. Castin, and K. Mølmer, Phys. Rev. Lett. **68**, 580 (1992).
[48] J. P. Gordon and A. Ashkin, Phys. Rev. A **21**, 1606 (1980).
[49] P. J. Ungar, D. S. Weiss, E. Riis, and S. Chu, J. Opt. Soc. Am. B **6**, 2058 (1989).
[50] O. Emile, R. Kaiser, C. Gerz, H. Wallis, A. Aspect, and C. Cohen-Tannoudji, J. Phys. II France **3**, 1709 (1993).
[51] G. K. Li, C. Hallas, and J. M. Doyle, New J. Phys. **27**, 043002 (2025).
[52] L. D. Augustovičová and J. L. Bohn, New J. Phys. **21**, 103022 (2019).